Authors
Zhou, Hao
Dai, Yining
Gregori, Giovanni
et al.

Automated morphometric measurement of the retinal pigment epithelium complex and choriocapillaris using swept source OCT

HAO ZHOU,[1] YINING DAI,[1] GIOVANNI GREGORI,[2] PHILIP R. ROSENFELD,[2] JACQUE L. DUNCAN,[3] DANIEL M. SCHWARTZ,[3] AND RUIKANG K. WANG[1,4,*]

[1]*Department of Bioengineering, University of Washington, Seattle, WA 98105, USA*
[2]*Department of Ophthalmology, Bascom Palmer Eye Institute, University of Miami Miller School of Medicine, Miami, FL 33136, USA*
[3]*Department of Ophthalmology, University of California, San Francisco, CA 94143, USA*
[4]*Department of Ophthalmology, University of Washington, Seattle, WA 98105, USA*
*wangrk@uw.edu

Abstract: We report the development of an automated method to measure morphological features of the retinal pigment epithelium (RPE), Bruch's membrane (BM) and choriocapillaris (CC) using a commercially available swept source OCT (SS-OCT) system. The locations of the inner segment/outer segment (IS/OS), RPE and CC were determined by optical coherence tomography (OCT) and OCT angiography (OCTA) A-scan intensity profiles, which were used to calculate the mean IS/OS-to-RPE distance, mean RPE-to-CC distance, mean RPE-to-CC outer boundary distance, mean RPE thickness and mean CC thickness across the entire scan volume. The automated method was tested on two groups of normal subjects: younger age group (n=20, 30.3 ± 5.72 years, axial length = 24.2 ± 0.96 mm) and older age group (n=20, 80.8 ± 4.12 years, axial length = 23.5 ± 0.93 mm). The 6×6 mm macular scans were acquired from one eye of each subject. Repeatability of the measurements showed a coefficient of variance < 5% for all the cases. CC locations were confirmed qualitatively with pixel-by-pixel moving of the *en face* OCT/OCTA images. Relative distance and thickness maps of the RPE-BM-CC complex were generated for visualization of regional changes. We observed thinner CC, thinner RPE and increased RPE-to-CC distance in the older age group. Correlation between CC thickness and choroid thickness suggests that the CC thins with the overall thinning of the choroid. These metrics should be useful to reveal more morphological details of RPE-BM-CC complex, provide a better understanding of the CC in three dimensions, and further investigate potential functional relationships between RPE, BM and CC, and their involvement in age-related ocular diseases.

1. Introduction

The retinal pigment epithelium (RPE)-Bruch's membrane (BM)-choriocapillaris (CC) complex undergoes alterations with aging and in disease.[1,2] The three components have an inter-dependent symbiotic relationship.[2] The RPE is a layer of densely packed hexagonal cells that are firmly attached to the anterior surface of Bruch's membrane. The RPE is needed for photoreceptor survival and metabolic exchange, it produces a variety of growth factors for both the photoreceptors and CC, and it forms the outer blood-retinal barrier.[3] The BM is an elastin- and collagen-rich extracellular matrix, serving as a molecular sieve.[4] Lying posterior to the BM is the CC, which is the terminal capillaries connecting the choroidal arteries and veins and responsible for the metabolic and oxygen needs of the overlying RPE and photoreceptors.[2,5]

Despite the importance of the RPE-BM-CC complex, few quantitative studies have reported their *in vivo* morphology, such as thicknesses, and how they change in aging or diseases. Histology

studies have measured the RPE thickness (14.1 μm) and BM thickness (2.0 - 4.7 μm) as well as CC diameter (9.8 μm).[6,7] However, these studies are limited in sample size, and measurements can be easily distorted during tissue processing. Optical coherence tomography (OCT) is a non-invasive and depth-resolved imaging technology that is widely used in routine ophthalmic practice.[8] *In vivo* OCT structural imaging provides visualization of the choroid and retinal layers comparable to histologic analysis (Fig. 1, reproduced with permission from [9] and [10]).
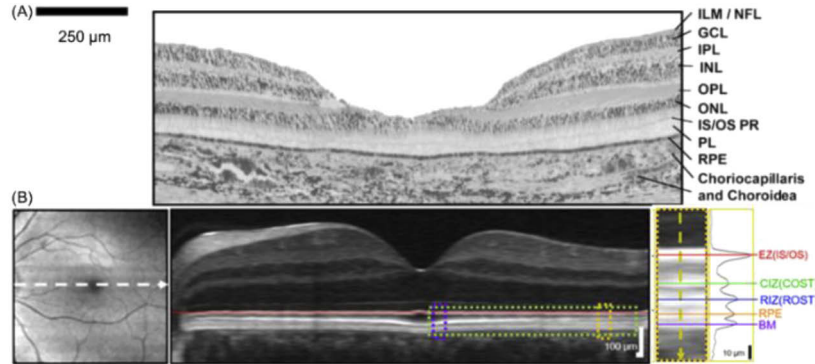
Fig. 1. The ability of OCT to image physiological features that correspond to layers observed in standard histological. Provided is an example comparison of (A) OCT image with (B) histologic micrograph of normal human macula. (Images were reproduced with permission from Ref. [9] and Ref. [10]). ILM: inner limiting membrane, NFL: nerve fiber layer, GCL: ganglion cell layer, IPL: inner plexiform layer, INL: inner nuclear layer, OPL: outer plexiform layer, ONL: outer nuclear layer, IS/OS PR: junction between the inner and outer segment of the photoreceptors, PL: plexiform layer, RPE: retinal pigment epithelium, EZ: ellipsoid zone, CIZ: cone interdigitation zone, COST: cone outer segments, RIZ: rod interdigitation zone, ROST: rod outer segment tips.

The reflectivity change in OCT structural scans has been investigated to identify the components in the RPE-BM complex. For example, the change in reflectivity was used to automatically segment retinal layer boundaries based on various methods like graph search and deep learning.[11,12] Thickness of RPE-BM complex in normal eyes was measured via spectral-domain OCT (SD-OCT) and the mean RPE-BM complex thickness was reported at 26.3 μm at the central fovea, and this value varies with age, ethnicity, refraction, intraocular pressure (IOP) and smoking.[13,14] A thicker RPE-BM complex (32.3 μm at central fovea) was associated with dry age-related macular degenerations (AMD) patients when compared to age-matched normal subjects.[15] Measurement of the CC thickness was attempted by Yiu et al. and Zhang et al. using SD-OCT [16,17] in which they used the OCT structural information based on reflectivity to identify the CC layer, and the distance between the outer boundary of RPE to the top surface of capillary vessels was defined as the "equivalent CC thickness". However, such a definition is debatable because it does not measure the CC thickness, but rather the distance of 'RPE and CC separation'. Since it is difficult to contrast the CC from the surrounding RPE tissue complex, it remains challenging to identify the CC precisely by using structural reflectivity on OCT B-scans alone.

The recent introduction of clinical swept source OCT (SS-OCT) is promising for imaging the RPE-BM-CC complex, especially the CC layer that is beneath RPE because of its advantages over the SD-OCT, which include deeper penetration and lower sensitivity fall-off.[18,19] In addition to structural OCT scans, OCT angiography (OCTA) has been introduced to extract flow signals from the CC layer.[20–22] These advancements in OCT imaging provide new opportunities to characterize the RPE complex and CC thickness *in vivo*.

While the features in OCT structural scans enable identification of the RPE, OCTA flow signals may have greater utility for localization of the CC since the CC is a dense network of flowing blood. Previously, *en face* OCT/OCTA images have been used to visualize RPE, CC and choroidal vessels, upon which the choroid and CC thickness were measured crudely by discretely counting the number of *en face* depth-pixels encompassed within each layer.[23] While such an approach is subjective, the CC thickness was measured to be $81.3 \pm 21.2\,\mu m$ in the younger group (mean age = 30.86) and $56.4 \pm 12.1\,\mu m$ in the older group (mean age = 54.83).[23] These measurements were much larger than the histological results probably due to the low sensitivity of the depth estimation on the *en face* images. Miller's group reported the use of adaptive optics OCT (AO-OCT) to characterize the CC morphology in which OCT/OCTA intensity profiles on A-scans were used to localize the peak positions that corresponded to the RPE and CC, respectively.[24] The distance between the RPE peak in the OCT profile and the CC peak in the OCTA profile were defined as 'RPE to CC separation' that was reported to be $19.5 \pm 2.6\,\mu m$.[24] Similarly, Zhou et al. also used A-scan profiles to locate the RPE and CC and reported a similar RPE to CC distance of around $20\,\mu m$ using a custom-built system.[25] However, while the RPE and CC locations were identified in the OCT and OCTA profiles, the RPE-to-CC distance measurements were made on single B-scans and no further measurements have been explored and reported.

Herein, we employ a commercially available SS-OCT and SS-OCTA instrument to explore the *in vivo* morphometric measurements of the RPE-BM-CC complex and propose an automatic method to measure the locations and thicknesses of the RPE, BM and CC layers within the whole scanning region. We tested the repeatability of the measurements and compared them between younger and older normal subjects. These metrics, obtained by combining the use of SS-OCT and SS-OCTA A-scans from patients' eyes, should be useful to reveal morphological *in vivo* details of the RPE-BM-CC complex. This approach should improve our understanding of the RPE-BM-CC complex in three dimensions and its involvement in ocular diseases.

2.   Method

2.1.   Image acquisition

The SS-OCT instrument (PlexElite 9000, Carl Zeiss Meditec Inc.) used in this study has a central wavelength of 1060 nm, a bandwidth of 100 nm, and a scanning rate of 100 kHz. Each A-scan was acquired over a depth of 3.0 mm in tissue, containing 1536 pixels. The device was characterized by a full-width at half maximal (FWHM) axial resolution of ~5 µm in tissue and a lateral resolution at the retinal surface estimated at ~16 µm. Each subject was scanned with a 6×6 mm macular scan pattern centered on the fovea. The scanning protocol was 500 A-scans per B-scan, repeated 2 times at each of the 500 B-scan positions, which resulted in a sampling grid with a separation of 12 µm. Three consecutive scans were obtained for assessment of intra-visit repeatability.

Images were acquired as part of a prospective OCT study approved by the University of Washington institutional review board (IRB). Consents were obtained from all subjects before scanning. All procedures adhered to the tenets of the Declaration of Helsinki. Subjects with any history of any ocular disease, any pathology detected during examination or on OCT imaging, axial length longer than 26.0 mm, a refractive error of greater than -6.0 diopters, or any history of uncontrolled hypertension or diabetes mellitus were excluded. For all enrolled subjects, the right eye was the default selection unless poor scan signal or gross eye movements were noted during scanning. At the time of enrollment, both axial length measurements and SS-OCTA imaging were performed on each subject. Axial length was measured using a noncontact biometry instrument (IOLMaster, Carl Zeiss Meditec Inc.). Images with significant media opacity, signal strength less than 7 as defined by the manufacturer, or severe motion artifact were excluded from the study.

2.2. OCT/OCTA profiles on A-scans

To generate OCT images, each A-scan was a Fourier transform of one OCT spectrum and the logarithmic intensity scale was used to display OCT images in order to emphasize weak scattering.[26] OCTA images were obtained using the complex optical microangiography (OMAG^C) algorithm, which utilized the variations in both intensity and phase information between sequential B-scans at the same location to isolate the motion signals.[27] This algorithm has demonstrated previously as being more robust when compared with other OCTA algorithms such as speckle-variance OCTA, phase-variance OCTA and split-spectrum phase-gradient OCTA.[21] The OCT/OCTA A-scans were aligned to the RPE segmentation. To do so, 3D OCT and OCTA scans were flattened at the RPE centerline.[10] To detect the RPE centerline, the local maxima of the OCT intensity gradient in each A-line was detected.[28] In each B-scan, a 7th degree polynomial was fitted and outliers were discarded. Finally, the RPE centerline was identified using a graph search method to find the shortest path connecting all the remaining nodes (the maximum intensity points after eliminating the outliers) and with their OCT intensities setting to be their corresponding weights (Fig. 2). [28] After the RPE positions were identified for all the A-scans [Fig. 2(A)], the 3D OCT and OCTA scans were finally flattened with the reference to these RPE positions by setting all the RPE positions at a fixed known pixel height within 3D scans [Fig. 2(B)].
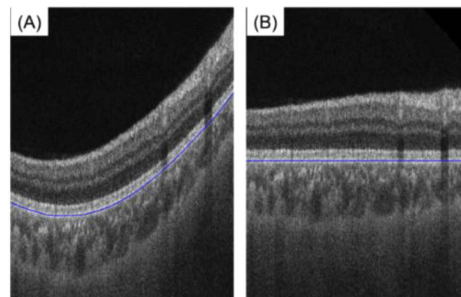
Fig. 2. Illustration of aligning OCT A-scans using the RPE position as a reference. After detecting the RPE centerline (blue line) (A), the OCT B-scans were flattened at the RPE centerline by setting all the RPE positions at a fixed known pixel height within 3D scans (B). The OCT/OCTA a-scan intensity profiles were then calculated by collapse-averaging all A-lines within the selected sub-regions.

From the flattened 3D scans, OCT/OCTA profiles of A-scans (along depth z direction) were obtained by collapse-averaging all the A-scans within a selected region of m x m pixels and normalized:

$$I_{OCT}(z) = \frac{\sum_m \sum_m I_{OCT}(x, y, z)}{m^2 max_{OCT}} \tag{1}$$

$$I_{OCTA}(z) = \frac{\sum_m \sum_m I_{OCTA}(x, y, z)}{m^2 max_{OCTA}} \tag{2}$$

Where I_{OCT} and I_{OCTA} are OCT/OCTA intensities of each spatial pixel position, while max_{OCT} and max_{OCTA} are the maximum values of each OCT/OCTA profile for normalization, respectively [Figs. 3(A)–3(D)].

2.3. En face mapping for distances and thickness of the RPE-BM-CC complex

After generating the OCT/OCTA profiles, a peak detection algorithm was developed to determine the position of the intensity peaks [Fig. 3(E)]. The interpretation of these peaks was determined based on previous histologic results [6,7] and AO-OCT results [24]. The relative depth locations
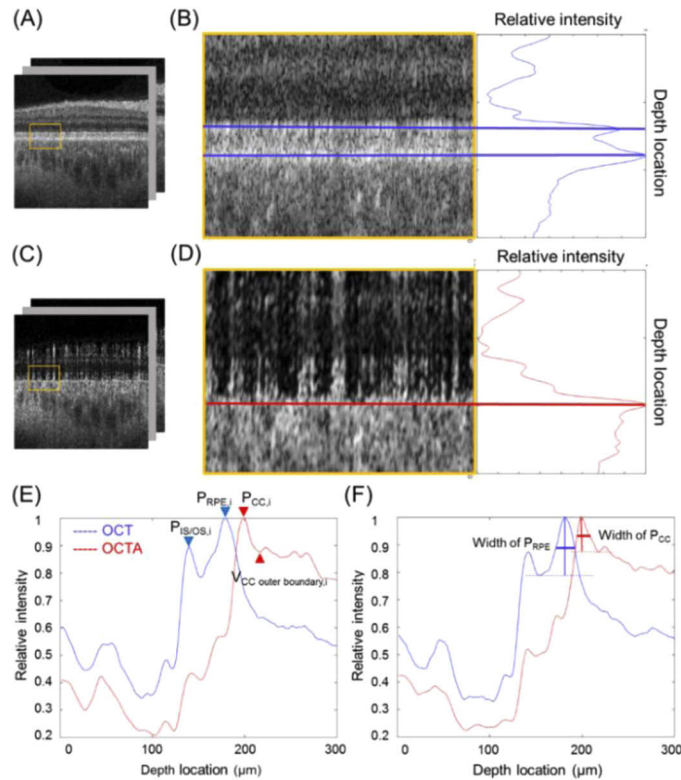
Fig. 3. Measuring location and thickness of RPE, BM and CC automatically using OCT and OCTA A-scans. (A-D) OCT and OCTA B-scans were first flattened using the reference of the RPE centerline (A,C) and A-scan signal intensity profiles along the depth were generated by calculating the collapsed-average of the aligned A-scans in the zoomed-in selected regions (yellow box), respectively (B,D). Blue lines indicate the location of IS/OS and RPE peak, respectively. Red lines indicate the location of CC peak. (E) Identification of OCT/OCTA peaks for IS/OS, RPE, CC and CC outer boundary. (F) Illustration of equivalent width measurement for RPE and CC peaks using the half maximum as reference.

of these peaks are shown on the x-axis and can be used to calculate the distances between layers as well as the thickness measurements [Figs. 3(E) and 3(F)] The measurements were conducted across the whole scanned region. Outliers that were three standard deviation below or above the mean were excluded from the calculation.

For each spatial location (pixel) in the *en face* image (500×500 pixels, 6×6 mm), OCT and OCTA A-scans in a 19×19 pixel [m=19 in Eqs. (1) and (2), 228×228 μm] sub-region were averaged to generate the OCT/OCTA intensity profile of the pixel at the center. Peak locations of the IS/OS and RPE were identified from the OCT intensity profile while that of the CC was identified from the OCTA intensity profile. The corresponding IS/OS-to-RPE distance, RPE-to-CC distance, RPE-to-CC outer boundary distance, RPE thickness and CC thickness were calculated based on the peak locations and widths as described above. Outliers, which were three standard deviation below or above the mean value of the whole map, were excluded. Finally, the *en face* mapping was generated through a P-spline method to fit the surface, which has been successfully used to fit the surface of choroid-sclera interface and macula.[28,29] The parameters used in P-spline fitting were 30 pixels for width, 0.5 (out of 0 ~ +∞) for penalties on the neighboring coefficients of the tensor products and one for weights.

2.4.   Metrics for the RPE-BM-CC complex

Using the same strategy as that for the *en face* mapping of RPE-BM-CC complex morphological features, we were able to calculate the following morphometric measurements of the RPE complex for the whole scanning region. Each B-scan was treated as individual selected region and OCT/OCTA profiles were generated from each B-scan. Mean values of all metrics were averaged from all B-scans in the entire volume. This largely reduced the calculation load and increased the processing speed when compared to the *en face* mapping (n=500 vs. n=500×500 for the number of individual measurements before averaging). There was no significant difference between the results averaged from all B-scans and that averaged from all 19×19-pixel square regions for the whole scan region (n=13, P=0.89). Furthermore, using individual B-scan to generate profile eliminates the artifact of subpixel misalignment between adjacent B-scans along slow-scan direction. [30]

Mean IS/OS to RPE distance is calculated as:

$$Mean\ IS/OS\ to\ RPE\ distance = \sum_{i=1}^{n}(P_{RPE,\ i} - P_{IS/OS,i})/n \qquad (3)$$

where $P_{RPE,i}$ and $P_{IS/OS,i}$ are the relative depth locations of RPE and IS/OS peaks in the OCT signal profile of the *ith* B-scan respectively, n is the total number of B-scans in the volume scan.

Mean RPE to CC distance is calculated as:

$$Mean\ RPE\ to\ CC\ distance = \sum_{i=1}^{n}(P_{CC,i} - P_{RPE,i})/n \qquad (4)$$

where $P_{CC,i}$ and $P_{RPE,i}$ are the relative depth locations of CC peak in the OCTA signal profile and RPE peak in the OCT signal profile of the *ith* B-scan respectively.

Mean RPE to CC outer boundary distance is calculated as:

$$Mean\ RPE\ to\ CC\ outer\ boundary\ distance = \sum_{i=1}^{n}(V_{CC\ outer\ boundary,i} - P_{RPE,i})/n \qquad (5)$$

where $V_{CC\ outer\ boundary,i}$ and $P_{RPE,i}$ are the relative depth locations of CC posterior valley, which indicated the ending of the CC peak in the OCTA signal profile and RPE peak in the OCT signal profile of the *ith* B-scan respectively.

Mean RPE and CC thicknesses were measured as the width of peaks using the half maximum as reference [Fig. 3(F)]. Full width at half maximum (FWHM) is an expression that is widely used in definition of bandwidth in spectrum-like curves and were used to compare width of waveform signals without any further complicated fitting.

$$Mean\ RPE\ thickness = \sum_{i=1}^{n} width\ of\ P_{RPE}\ /n \qquad (6)$$

$$Mean\ CC\ thickness = \sum_{i=1}^{n} width\ of\ P_{CC}/n \qquad (7)$$

2.5.   Measurement of the mean choroid thickness

Mean choroid thickness (MCT) was measured using our previously developed automated method. [28] Briefly, attenuation correction ('Gain Control') was applied to OCT B-scans to enhance the contrast at choroidal-sclera-interface. Then the bottom of choroidal large vessels was segmented based on the intensity gradient and the surface was fitted using the P-spline method described above. The distance between the segmented RPE and the outer boundary of choroidal vessels was averaged to calculate the MCT for each 3D scan.

3.   Results

En face images of OCT and OCTA scans have been reported previously to show the morphological differences between different layers and qualitatively determine the locations of the RPE and

CC. [23] It is clinically important to qualitatively check whether the peak locations identified from OCT/OCTA intensity profiles correspond to the anatomic layers. For this reason, we also generated *en face* OCT and OCTA images (Fig. 4). Figures 4(B) and 4(C) are the *en face* OCT and OCTA images of the selected slab (10 μm) centered at the IS/OS peak [green box in Fig. 4(A)]. Figures 4(D) and 4(E) are the *en face* OCT and OCTA images of the selected slab centered at the RPE peak [blue box in Fig. 4(A)], whereas Figs. 4(F) and 4(G) are the *en face* OCT and OCTA images of the selected slab centered at the CC peak [red box in Fig. 4(A)]. Both IS/OS and RPE layers showed homogeneous, hyper-reflective layers with only "shadowing" from retinal vessels in OCT images and retinal vasculature in OCTA images. We observed CC vasculature patterns only appeared in the OCTA slabs centered at the CC peak [Fig. 4(G)], which confirmed our hypothesis that the identified CC peak in OCTA intensity profile indicates the location of CC layer.
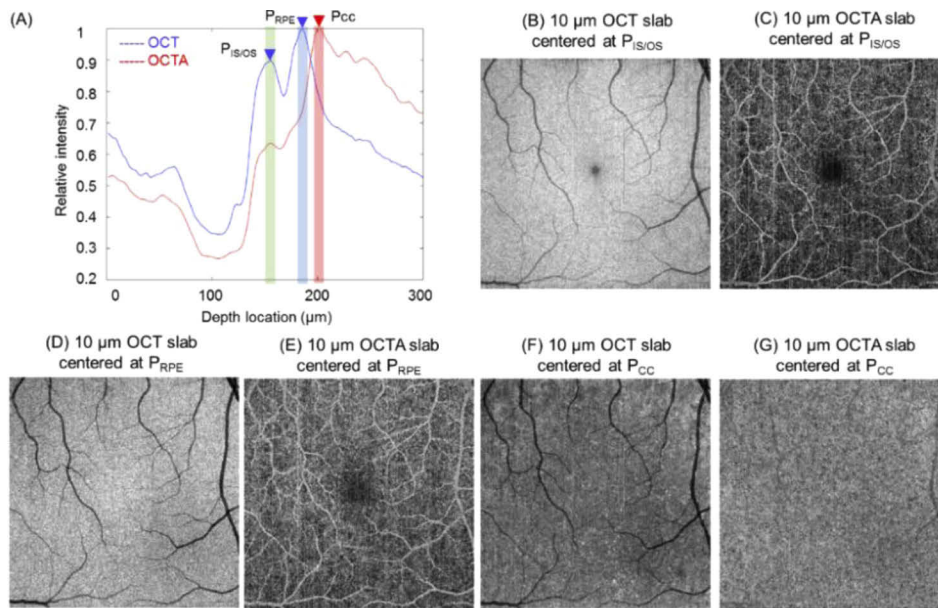

Fig. 4. *En face* images of 10 μm OCT/OCTA slabs centered at $P_{IS/OS}$, P_{RPE} and Pcc respectively. (A) Representative OCT and OCTA intensity profiles with 10 μm slabs centered at $P_{IS/OS}$ (green box), P_{RPE} (blue box) and Pcc (red box). (B,C) OCT and OCTA *en face* images of the 10 μm slabs cantered at $P_{IS/OS}$. (D,E) OCT and OCTA *en face* images of the 10 μm slabs cantered at P_{RPE}. (F,G) OCT and OCTA *en face* images of the 10 μm slabs cantered at P_{CC}.

To further confirm the location and boundary of RPE and CC layer indicated by the OCT/OCTA intensity profile, more *en face* OCT and OCTA images (Fig. 5) were generated through a sum projection of 10μm-thick slabs at various depths with a reference to the identified RPE peak (P_{RPE}), CC peak (P_{CC}) and CC valley of outer boundary (Vcc). Figures 5(A1)-5(A5) show representative locations of the two slabs above and below P_{RPE} and their corresponding OCT/OCTA *en face* images. Both slabs showed a homogeneous, hyper-reflective layer with only "shadowing" from retinal vessels in the OCT images [Figs. 5(A2) and 5(A4)] and the retinal vasculature, which are the retinal projection artifacts on the OCTA *en face* images [Figs. 5(A32) and 5(A5)] and were in good agreement with the observations at the level of the RPE layer reported previously.[23] Figs. 5(B1)–5(B5) show representative locations of the two slabs above and below P_{CC} and their corresponding OCT/OCTA *en face* images. In the slab that is 10 μm above Pcc, the OCT *en face* image shows typical RPE structure while the OCTA *en face* image shows dense uniform

vasculature in the CC overlaid with projection artifacts from superficial retinal vessels [Figs. 5(B2) and 5(B3)]. Slabs of $10\,\mu m$ below *Pcc* showed a reticular pattern that was lying external to the RPE in OCT images and CC vasculature pattern in OCTA images [Figs. 5(B4) and 5(B5)]. The reticular pattern is less homogeneous than RPE layer because both the CC and other microvascular structures appear as a complex reticular pattern.[23] Figs. 5(C1)–5(C5) showed representative locations of the two slabs above and below V_{CC} and their corresponding OCT/OCTA *en face* images. *Vcc*, which is the ending of the CC OCTA peak, is considered as the outer boundary of CC. The following peaks at deeper locations in the OCTA profile might come from the vessels in the deeper layer, speckle noise, or the choroidal-scleral boundary (C1). The $10\,\mu m$ slab above the *Vcc* showed similar a reticular pattern in both the OCT structure image and the CC vasculature image in OCTA [Figs. 5(C2) and 5(C3)]. In contrast, the $10\,\mu m$ slab below *Vcc* started to show patterns of larger choroidal vessels which is an interwoven pattern with short segments crossing each other and the vessel size is larger than the CC image [Figs. 5(C4) and 5(C5)], which are the typical appearance in the Sattler's layer.
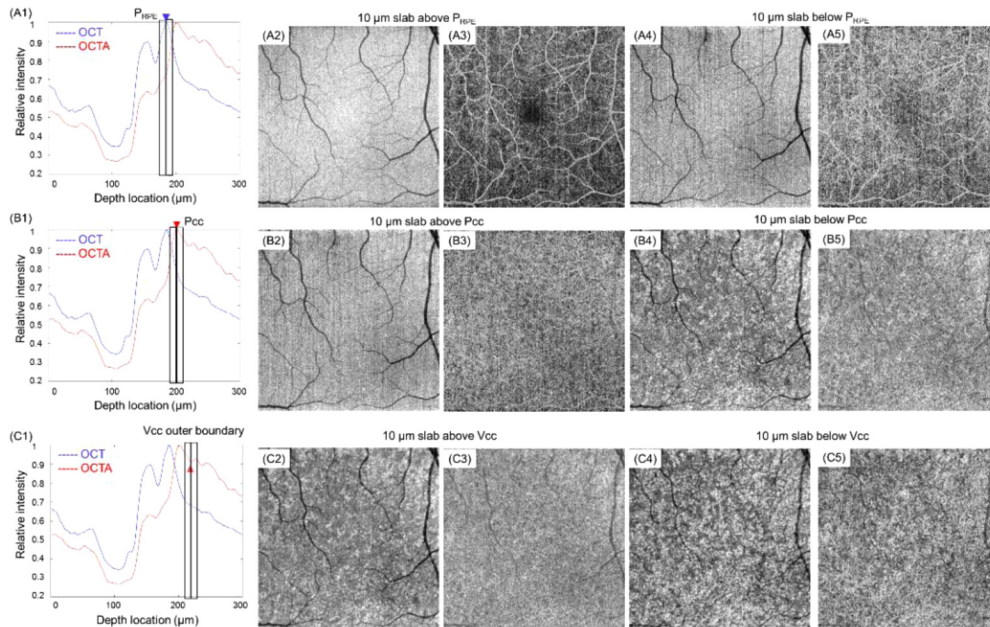
Fig. 5. *En face* images of selected $10\,\mu m$ slabs above and below the P_{RPE}, *Pcc* and *Vcc*. (A1) Representative OCT and OCTA intensity profiles with $10\,\mu m$ slabs selected above and below P_{RPE}. (A2, A3) OCT and OCTA *en face* images of the $10\,\mu m$ slabs above P_{RPE}. (A4, A5) OCT and OCTA *en face* images of the $10\,\mu m$ slabs below P_{RPE}. (B1) Representative OCT and OCTA intensity profiles with $10\,\mu m$ slabs selected above and below *Pcc*. (B2, B3) OCT and OCTA *en face* images of the $10\,\mu m$ slabs above *Pcc*. (B4, B5) OCT and OCTA *en face* images of the $10\,\mu m$ slabs below *Pcc*. (C1) Representative OCT and OCTA intensity profiles with $10\,\mu m$ slabs selected above and below *Vcc*. (C2, C3) OCT and OCTA *en face* images of the $10\,\mu m$ slabs above *Vcc*. (B4, B5) OCT and OCTA *en face* images of the $10\,\mu m$ slabs below *Vcc*.

These observations agree well with the previous reports about morphological and vascular features of the RPE, CC and Sattler's layer [5,7,23,31]. Given the fact that human chorioretinal layers are complicated and there is no distinct anatomic boundary for the CC since vessel calibers change in a progressive gradient, it is still challenging to confirm the boundaries between layers from OCT imaging. By determining the peaks of signals, however, we were able to at least closely

localize the central locations of each layer and evaluate their relative locations and thicknesses. The metrics we propose may provide the ability to perform quantitative comparisons to reveal the relative morphological changes in the RPE-BM-CC complex during normal aging and in retinal diseases.

We tested the repeatability of all the proposed morphometric measurements (defined in Section 2.4) on 13 normal subjects (Mean age = 47.2 ranging from 27 to 82; 6/13 are male). In these 13 subjects, three consecutive macular scans were obtained to test repeatability. The coefficient of variance (CV) of three repeated scans ranged from 1.06-2.52% (Table 1).

Table 1. Average, standard deviation (SD) and coefficient of variance of all metrics measured from 13 normal eyes (Age ranging from 27 to 82) with three repeated scans.

	Average ± SD [1st Scan, µm]	Average ± SD [2nd Scan, µm]	Average ± SD [3rd Scan, µm]	coefficient of variation (**CV**)
Mean IS/OS to RPE distance	38.8 ± 4.50	39.4 ± 4.47	39.2 ± 4.09	2.23 ± 2.16 %
Mean RPE to CC distance	19.6 ± 1.05	19.7 ± 0.909	19.8 ± 1.08	1.06 ± 0.77 %
Mean RPE to CC outer boundary distance	37.2 ± 2.86	37.2 ± 2.91	37.6 ± 3.20	1.65 ± 1.12 %
Mean RPE thickness	23.8 ± 3.19	24.5 ± 3.22	24.0 ± 2.76	2.52 ± 2.33 %
Mean CC thickness	13.1 ± 2.11	13.1 ± 2.15	13.1 ± 2.44	2.03 ± 1.19 %

Twenty normal subjects with younger ages (50% female, age = 30.3 ± 5.72 years, axial length = 24.2 ± 0.96 mm) and twenty with older ages (50% female, age = 80.8 ± 4.12 years, axial length = 23.5 ± 0.93 mm) were recruited and 6 mm x 6 mm macular scans were acquired of one normal eye from each subject. Figure 6 shows the representative OCT/OCTA B-scans and intensity profiles of a normal eye from a younger subject and a normal eye from an older subject. In both cases, peak locations of the RPE and CC were identified in the OCT and OCTA A-scan intensity profiles [Figs. 6(C) and 6(D)].
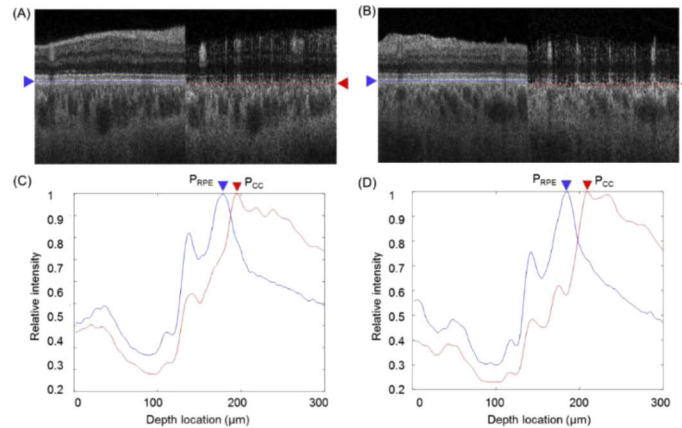
Fig. 6. Representative OCT and OCTA B-scans with intensity profiles indicating RPE and CC locations from a younger and an older subject, respectively. (A) Representative OCT and OCTA B-scans with marked lines indicating RPE location (blue line) and CC location (red line) of a normal eye from a 30-year-old female subject. (B) Representative OCT and OCTA B-scans with marked lines indicating RPE location (blue line) and CC location (red line) of a normal eye from an 80-year-old female subject. (C) OCT/OCTA intensity profiles of the corresponding B-scans shown in (A). (D) OCT/OCTA intensity profiles of the corresponding B-scans shown in (B).

En face mapping of the distances for the RPE-BM-CC complex would be useful to investigate regional changes in the geometry of the RPE-BM-CC complex (Fig. 7). The measurement of the RPE-BM-CC complex at various regions can be performed by selecting A-scans in the region-of-interest. By selecting a small *en face* moving window of 19×19 pixels, we were able
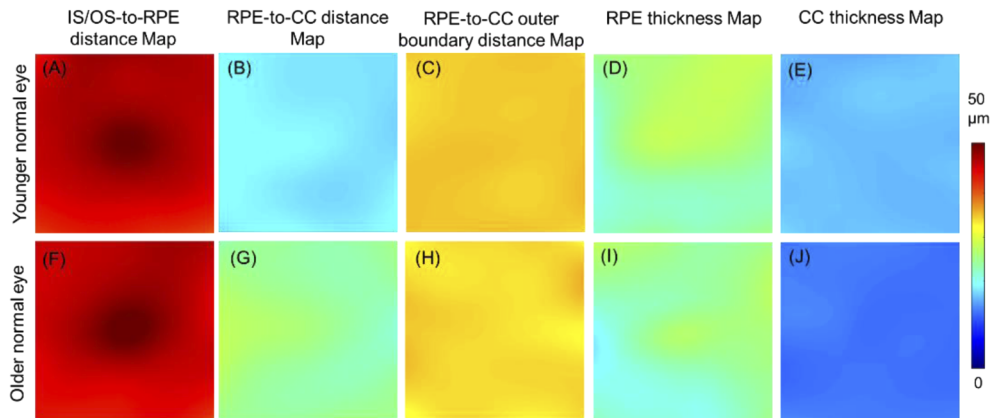
Fig. 7. *En face* mapping of IS/OS to RPE distances (A&F), RPE to CC distances (B&G), RPE to CC outer boundary distances (C&H), RPE thicknesses (D&I) and CC thicknesses (E&J) of normal eyes from a 27-year-old female and a 81-year-old female, respectively. All the *en face* mappings are using the same color-coded scale of 50 μm. Subtle changes may be revealed better by selecting narrower scale for an individual map like the CC thickness map.
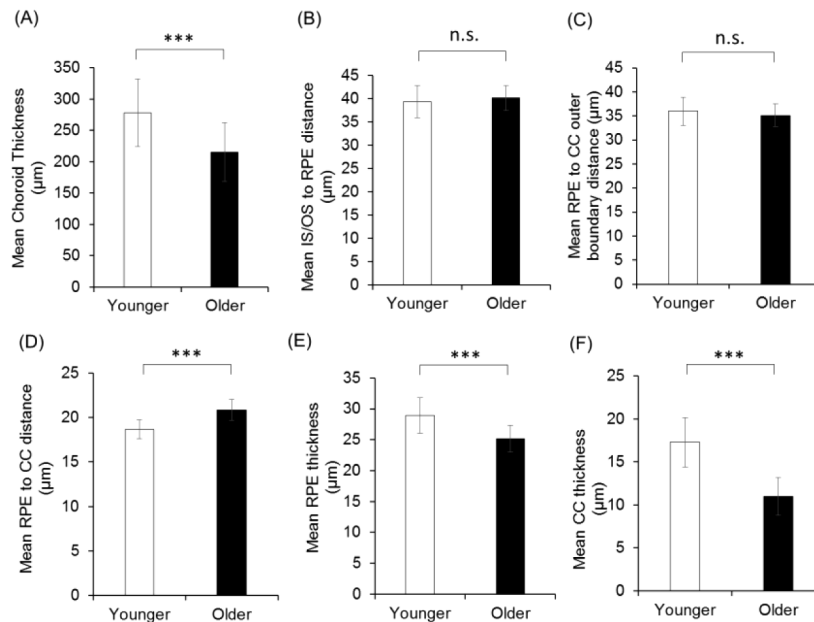
Fig. 8. Metrics of mean choroid thickness (A), mean IS/OS to RPE distance (B), mean RPE to CC outer boundary distance (C), mean RPE to CC distance (D), mean RPE thickness (E) and mean CC thickness (F) of normal eyes from subjects in younger and older groups. Data is represented as mean ± SD (n=20). Student's t-test was applied for statistical analysis (n.s.: not significant; *: P<0.05; **: P<0.01; ***: P< 0.001).

to measure RPE-BM-CC complex at small regions and generate *en face* maps of all the metrics. The use of color-coded values to represent the distances between layers or the thicknesses of layers can help in the visualization and comparison of these layers. For example, the elevation of the IS/OS layer at the fovea was observed in normal eyes in both younger and elderly subjects [Figs. 7(A) and 7(F)]. The RPE-to-CC distance was larger across the whole region in the eye of the older subject [Figs. 7(B) and 7(G)] while RPE thickness map [Figs. 7(D) and 7(I)] and CC thickness map [Figs. 7(E) and 7(J)] was relatively homogeneous and was thinner in the eye of the older subject across the whole region. We would expect such *en face* mapping to be more useful in the visualization of the morphology changes of the RPE-BM-CC complex in pathological cases.

In this study, the statistical analysis was done on the averaged measurements throughout the entire 6×6 mm scanning region, which neglected the regional variances. All mean metrics were measured and averaged from individual B-scans within the 3D scan region and compared between normal eyes from younger and older subjects (Fig. 8). Mean choroid thickness was significantly smaller in eyes from the older group (278.3 ± 54.1 µm) than from the younger group (215.6 ± 47.0 µm) (P=0.0005, ***). There were no significant differences in the measurements of the mean IS/OS to RPE distance nor in that of the mean RPE to CC outer boundary distance in the younger and older groups. The mean CC outer boundary was approximately 35.5 µm below the RPE centerline regardless of age [Fig. 8(C)]. We observed a larger RPE-to-CC distance in the older groups [Fig. 8(D)], which agrees with previous AO-OCT measurements.[24] Mean RPE
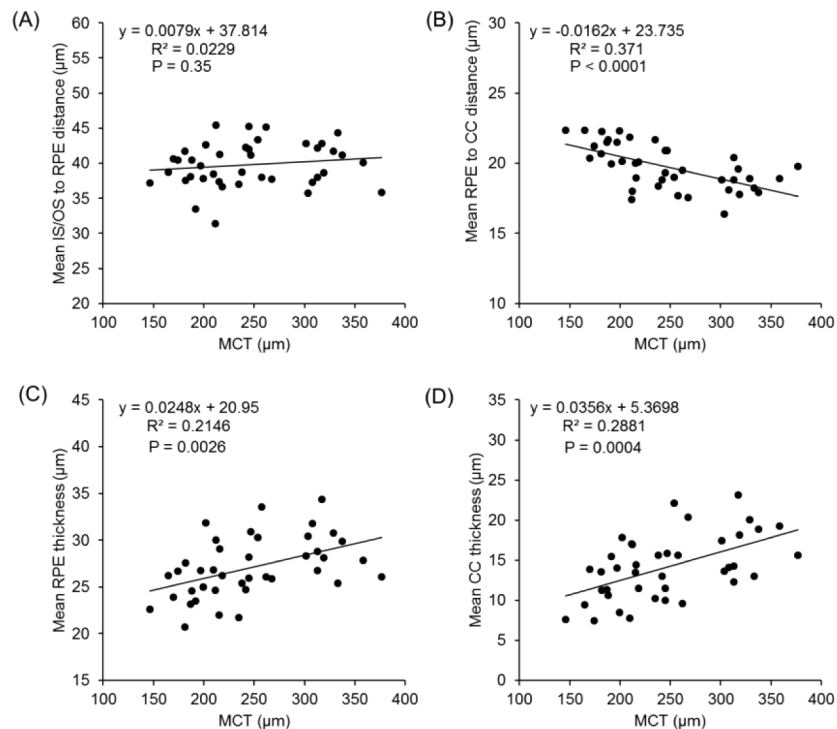
Fig. 9. Correlations between the metrics of the RPE-BM-CC complex and mean choroid thickness (MCT). (A-D) Correlations between MCT and the metrics of RPE-BM-CC complex (mean IS/OS to RPE distance, mean RPE to CC distance, mean RPE thickness and mean CC thickness). Data was analyzed through Pearson's correlation analysis. MCT: mean choroidal thickness.

thickness and mean CC thickness were both thinner in normal eyes from the older group (both P < 0.0001).

It has been reported that the choroid becomes thinner with aging.[32] It might also be interesting to investigate the correlation between the choroid and the RPE-BM-CC complex. Pearson's correlation analysis was applied to study the correlation between the metrics of RPE-BM-CC complex and mean choroid thickness (MCT) (Fig. 9). Mean RPE to CC outer boundary distance varies little regardless of MCT, nor age. Mean IS/OS to RPE distance was not correlated with MCT either. Mean RPE to CC distance was negatively correlated with MCT, while mean RPE thickness and mean CC thickness were positively correlated with MCT (all P<0.01). Mean CC thickness showed a linear relationship with MCT following the equation of 0.0356x + 5.4 µm where x is the measured mean thickness of the choroid [Fig. 9(D)].

4.　Discussion

We have described an automated method that utilizes OCT and OCTA signals in A-scans to locate and measure the thicknesses of three major components in RPE-BM-CC complex. The method aligned the A-scans at the RPE level, and the OCT/OCTA intensity profiles along the depth direction were subsequently generated by calculating the collapse-averaged A-scan signals within a region of interest. The intensity peaks corresponding to the locations of IS/OS, RPE and CC were automatically identified from the OCT/OCTA profiles, respectively, by the use of a peak-finding algorithm. Finally, the relative locations and thicknesses evaluated from the identified peaks were interpolated using P-splines and visualized as *en face* maps (Fig. 7) to show the regional variations or the whole scan region was averaged from B-scans of the entire scan region (Fig. 8). Using this automated algorithm, we found that the mean RPE and CC thicknesses were thinner in normal eyes in the older age group compared to the younger age group, and they were positively correlated with the mean choroidal thickness. The RPE-to-CC distance, or equivalently the thickness of RPE-BM-CC complex, was increased in normal eyes in older subjects and was negatively correlated with the mean choroid thickness.

To the best of our knowledge, the locations and thicknesses of the RPE-BM-CC complex have not been evaluated using commercial SS-OCT/OCTA devices as we have done here. Comparing with previous histology and *in vivo* imaging studies, RPE to CC distance is the same metric that has been previously reported as the 'RPE-to-CC separation'. This includes the RPE complex and the avascular regions between Bruch's membrane and CC anterior surface. AO-OCT measurements showed an averaged RPE-to-CC separation across subjects and retinal eccentricities to be 17.5 ± 2.1 µm.[24] In several studies using SD-OCT, researchers have been using 30 µm as RPE-to-CC separation in the standard setting of the SD-OCT software.[33,34] Our measurements showed an average RPE-to-CC distance across whole 6 mm × 6 mm scan region to be 18.7 ± 1.1 µm in younger group and 20.9 ± 1.2 µm in older group, which agrees well with the AO-OCT results. The thickness of BM is not directly observed, segmented and measured, because it is difficult to be separated from the RPE layer in normal cases, however, the changes in BM thickness may be reflected or indicated by the metric of RPE-to-CC distance. RPE thickness was measured to be around 11 µm in histology studies [7,35], 17.5 µm using AO-OCT [24], and 26.3 ± 4.8 µm using SD-OCT [13]. Using SS-OCT, we measured RPE thickness to be 28.9 ± 2.9 in younger group and 25.1 ± 2.2 µm in older groups, which is closer to the range of results by SD-OCT. The differences are likely due to sample handling and preparation in histology and anatomical interpretation of the reflectance peaks in the RPE of SS-OCT images. With a better capability of imaging CC in SS-OCT, we correlated morphology features of the RPE, BM, and CC together in clinical settings. These quantitative measurements of the RPE-BM-CC complex may be useful in the theoretical model developments that are aimed to investigate the ocular oxygen/nutrition supplies from the choroid to the photoreceptors, and the potential relationship

between the accumulation of deposits in the BM, chorioretinal vascular integrity, and visual function measurements.

The ability of the proposed automated identification of CC location and thickness has potential implications for current clinical investigations of choriocapillaris perfusion. Although numerous studies have demonstrated CC imaging with OCTA [31,33,34,36–38], the location and thickness of CC have not been evaluated and specified as reported herein. Due to the limitations of the current commercial devices, the bright and hyper-reflective RPE is often used as a reference to infer the location of the CC. Usually, once the RPE is identified, a fixed off-set is used to identify the anterior surface of the CC, yet most studies do not specify the depth of CC.[31,37,38] Based on our measurements, the RPE-to-CC distance increases with increasing thickness of the choroid, which indicates that a fixed off-set from the RPE might fail to accurately locate the CC inner surface. On the other hand, the CC outer boundary is difficult to delineate because of the vascular nature of choroid layers. Thus, a fixed thickness of 10, 20 or 30 μm, which has been used to segment CC slab in SS-OCTA or SD-OCTA imaging, [33,34,38–40] may not be the appropriate strategy. Therefore, the use of the CC locations identified by OCT/OCTA intensity profile from A-scans should be considered to identify the location of the CC layer for more accurate investigation of choriocapillaris perfusion.

Here in our current work, the CC outer boundary is shown by using the OCTA A-line intensity profile as the ending of the CC peak, which we believe might indicate the interface of CC and the medium-sized vessels in Sattler's layer. According to the OCTA signal profile with depth, it is clear that the majority of the flow signal is within the CC peak, and according to our measurements of CC thickness, the width of CC peak in OCTA imaging was averaged to 17.3 ± 2.6 μm in younger group and 11.0 ± 2.1 μm in older group and is positively correlated with choroidal thickness. This indicates a shrinkage of CC layer when the choroid is thinned. Thus, with the information of the RPE-to-CC outer boundary distance being constant among the subjects, we recommend that a segmentation strategy for imaging the CC would be 1) the ending position of the posterior surface of the CC is 35 μm below the identified RPE centerline for normal subjects, and 2) the thickness of the CC is selected according to the equation $0.0356x + 5.4$ μm where x is the measured mean thickness of the choroid. For example, if the thickness of the choroid is 300 μm in younger age, then the CC thickness should be 15 μm. While in the older age group, if the thickness of the choroid is 150 μm, then the CC thickness should be ~ 10 μm.

Furthermore, the morphological features of CC thickness and its separation from BM/RPE may provide more features on the depth direction in addition to *en face* image analysis. In pathological cases like geographic atrophy and myopia, the choroid has been reported to be less than half of the thickness of the choroid in age-matched normal eyes.[41,42] Our preliminary results suggest a positive correlation between CC and choroid thickness and a negative correlation between RPE-to-CC distance and choroidal thickness. It will be interesting to investigate whether there is also CC shrinkage and BM thickening in these pathologies associated with thinner choroids. Such changes may further suggest potential relationships between ocular oxygen/nutrition supplies, waste removal by RPE, deposit accumulation within BM and vascular functions of the CC.

The measurement of the RPE-BM-CC complex at various regions can be performed by selecting A-scans in the region-of-interest. Currently, the statistical analysis was done on the averaged measurements throughout the whole 6 mm × 6 mm scanning region which neglected the regional variances. For example, the IS/OS junction line is elevated at fovea in normal eyes, which appears like a dome over the foveola.[43] IS/OS to RPE distance is therefore supposed to be larger at the fovea compared with the peripheral regions, which is presented in the *en face* mapping of IS/OS-to-RPE distance maps [Figs. 7(A) and 7(F)] CC diameter has also been reported to be smaller in the macular regions and becomes larger in equatorial regions.[44,45] However, within the 6×6 mm scan, we did not observe obvious change in CC thickness with

regard to distance from the central macula [Figs. 7(E) and 7(J). Future studies at more peripheral location may be needed to reveal the variances.

There are several limitations of the proposed method. Firstly, the A-scans in the regions of interest were averaged to obtain the OCT/OCTA intensity profile along its depth. Single A-scan measurements are not adequate because in regions of flow voids where there is no CC flow, there will be no CC peak in the OCTA profile. Therefore, we used a sub-region to generate OCT-OCTA profiles for the center pixel in *en face* mapping. The size of the sub-region needs to be optimized to be large enough to eliminate single A-scan variance while small enough to differentiate regional distribution. For example, the CC loss has been implicated by various histopathologic studies as an initial factor for the development of pathologies like AMD.[46] We would expect challenges in detecting CC peak of the corresponding OCTA profiles from optimized sub-regions. Therefore, we suggest to either exclude the lesion where CC is completely lost or increase the size of the sub-region when dealing with pathologic eyes like AMD. Secondly, the RPE and CC thicknesses were defined as the width of the RPE and CC peaks at half maximum, respectively. These FWHM measurements will be smaller than those when measuring from the starting point to the ending point of the peaks, however, the half-maximum-width definition is more stable in case when the peak does not have a perfect 'Gaussian' shape. Furthermore, since the OCT and OCTA signals are displayed at logarithmic scale after Fourier transform [47], the half-maximum-width definition actually covers more than 90% of the signals within a 'Gaussian' shaped peak. Thirdly, the method needs to be adjusted for eyes with macular pathology. For example, the BM, instead of RPE centerline, should be used as the reference in eyes with elevated RPE from drusen. Regions with neovascularization should be excluded from the analysis since the CC OCTA signals are mixed with signals from new vessels. In highly myopic eyes, the thickness measurements of RPE-BM-CC layers could be affected due to axial elongation as the disease develops [48]. In this case, sub-regions or even single acquisition points (for example sub-fovea) should be used for thickness analysis. Furthermore, peripheral refractive errors have been reported in myopic, emmetropic and hyperopic subjects, [49] which should also be taken into consideration when applying the proposed method.

5. Conclusion

We have reported an automated method that utilizes OCT and OCTA A-scans to locate and measure the morphology of each component within RPE-BM-CC complex across the entire scanned region. Using this automated method, we found it is possible to provide *en face* mapping of the distances between layers and the thicknesses of RPE-BM-CC complex components. Compared with the younger aged normal group, we observed that the CC and RPE become thinner while the RPE-to-CC distance increases in an elderly aged group. The strong correlation between the CC thickness and choroidal thickness suggested that the CC thickness diminishes with the thinning of the entire choroid. We anticipate that these metrics will be useful to reveal more morphological details of RPE-BM-CC complex and provide better understanding of CC in three dimensions, which would help our endeavor in the current clinical investigations of potential functional relationships between RPE, BM and CC, and their involvement in macular disease.

Funding

Disclosures

Dr. Gregori, Dr. Rosenfeld and Dr. Wang received research support from Carl Zeiss Meditec, Inc. Dr. Gregori and the University of Miami co-own a patent that is licensed to Carl Zeiss Meditec, Inc. Dr. Rosenfeld is a consultant for Apellis, Boehringer-Ingelheim, Carl Zeiss Meditec, Chengdu Kanghong Biotech, Ocunexus Therapeutics, Hemera Biosciences, F. Hoffmann-La Roche Ltd., Isarna Pharmaceuticals, Ocunexus, Ocudyne, and Unity Biotechnology. Dr. Rosenfeld has equity interest in Apellis, Verana Health, and Ocudyne. Dr. Duncan is a consultant for AGTC, California Institute for Regenerative Medicine, Foundation Fighting Blindness, Editas Medicine, Ionis Pharmaceuticals, Novelion Therapeutics, ProQR Therapeutics, SparingVision, Spark Therapeutics. Dr. Duncan also receives research support from Foundation Fighting Blindness, Neurotech USA, Inc. Dr. Wang discloses intellectual property owned by the Oregon Health and Science University and the University of Washington. Dr. Wang also receives research support from Tasso Inc, Moptim Inc, and Colgate Palmolive Company. He is a consultant to Insight Photonic Solutions and Carl Zeiss Meditec. Dr. Zhou, Dr. Dai and Dr. Schwartz declare no conflicts of interest.

References

1. H. Ida, K. Ishibashi, K. Reiser, L. M. Hjelmeland, and J. T. Handa, "Ultrastructural aging of the RPE-Bruch's membrane-choriocapillaris complex in the D-galactose-treated mouse," Invest. Ophthalmol. Visual Sci. **45**(7), 2348–2354 (2004).
2. I. Bhutto and G. Lutty, "Understanding age-related macular degeneration (AMD): Relationships between the photoreceptor/retinal pigment epithelium/Bruch's membrane/choriocapillaris complex," Mol. Aspects Med. **33**(4), 295–317 (2012).
3. O. Strauss, "The retinal pigment epithelium in visual function," Physiol. Rev. **85**(3), 845–881 (2005).
4. B. D. Kels, A. Grzybowski, and J. M. Grant-Kels, "Human ocular anatomy," Clin Dermatol **33**(2), 140–146 (2015).
5. H. G. Ring and T. Fujino, "Observations on the anatomy and pathology of the choroidal vasculature," Arch. Ophthalmol. **78**(4), 431–444 (1967).
6. R. S. Ramrattan, T. L. van der Schaft, C. M. Mooy, W. C. de Bruijn, P. G. Mulder, and P. T. de Jong, "Morphometric analysis of Bruch's membrane, the choriocapillaris, and the choroid in aging," Invest. Ophthalmol. Visual Sci. **35**, 2857–2864 (1994).
7. C. A. Curcio, J. D. Messinger, K. R. Sloan, A. Mitra, G. McGwin, and R. F. Spaide, "Human Chorioretinal Layer Thicknesses Measured in Macula-wide, High-Resolution Histologic Sections," Invest. Ophthalmol. Visual Sci. **52**(7), 3943–3954 (2011).
8. J. M. Schmitt, "Optical coherence tomography (OCT): A review," IEEE J. Sel. Top. Quantum Electron. **5**(4), 1205–1215 (1999).
9. W. Drexler, U. Morgner, R. K. Ghanta, F. X. Kartner, J. S. Schuman, and J. G. Fujimoto, "Ultrahigh-resolution ophthalmic optical coherence tomography," Nat. Med. **7**(4), 502–507 (2001).
10. C. D. Lu, B. Lee, J. Schottenhamml, A. Maier, E. N. Pugh, and J. G. Fujimoto, "Photoreceptor Layer Thickness Changes During Dark Adaptation Observed With Ultrahigh-Resolution Optical Coherence Tomography," Invest. Ophthalmol. Visual Sci. **58**(11), 4632–4643 (2017).
11. S. J. Chiu, X. T. Li, P. Nicholas, C. A. Toth, J. A. Izatt, and S. Farsiu, "Automatic segmentation of seven retinal layers in SDOCT images congruent with expert manual segmentation," Opt. Express **18**(18), 19413–19428 (2010).
12. L. Fang, D. Cunefare, C. Wang, R. H. Guymer, S. Li, and S. Farsiu, "Automatic segmentation of nine retinal layer boundaries in OCT images of non-exudative AMD patients using deep learning and graph search," Biomed. Opt. Express **8**(5), 2732–2744 (2017).
13. F. Ko, P. J. Foster, N. G. Strouthidis, Y. Shweikh, Q. Yang, C. A. Reisman, Z. A. Muthy, U. Chakravarthy, A. J. Lotery, P. A. Keane, A. Tufail, C. M. Grossi, P. J. Patel, and U. B. E. V. Consortium, "Associations with Retinal Pigment Epithelium Thickness Measures in a Large Cohort Results from the UK Biobank," Ophthalmology **124**(1), 105–117 (2017).
14. J. Harris, Y. Subhi, and T. L. Sorensen, "Effect of aging and lifestyle on photoreceptors and retinal pigment epithelium: cross-sectional study in a healthy Danish population," Pathobiol. Aging Age-Relat. Dis. **7**(1), 1398016 (2017).
15. M. Karampelas, D. A. Sim, P. A. Keane, V. P. Papastefanou, S. R. Sadda, A. Tufail, and J. Dowler, "Evaluation of retinal pigment epithelium-Bruch's membrane complex thickness in dry age-related macular degeneration using optical coherence tomography," Br. J. Ophthalmol. **97**(10), 1256–1261 (2013).
16. L. Zhang, K. Lee, M. Niemeijer, R. F. Mullins, M. Sonka, and M. D. Abramoff, "Automated Segmentation of the Choroid from Clinical SD-OCT," Invest. Ophthalmol. Visual Sci. **53**(12), 7510–7519 (2012).

17. G. Yiu, Z. Wang, C. Munevar, E. Tieu, B. Shibata, B. Wong, D. Cunefare, S. Farsiu, J. Roberts, and S. M. Thomasy, "Comparison of chorioretinal layers in rhesus macaques using spectral-domain optical coherence tomography and high-resolution histological sections," Exp. Eye Res. **168**, 69–76 (2018).

18. A. R. Miller, L. Roisman, Q. Q. Zhang, F. Zheng, J. R. D. Dias, Z. Yehoshua, K. B. Schaal, W. Feuer, G. Gregori, Z. D. Chu, C. L. Chen, S. Kubach, L. An, P. F. Stetson, M. K. Durbin, R. K. K. Wang, and P. J. Rosenfeld, "Comparison Between Spectral-Domain and Swept-Source Optical Coherence Tomography Angiographic Imaging of Choroidal Neovascularization," Invest. Ophthalmol. Visual Sci. **58**(3), 1499–1505 (2017).

19. A. I. Dastiridou, E. Bousquet, L. Kuehlewein, T. Tepelus, D. Monnet, S. Salah, A. Brezin, and S. R. Sadda, "Choroidal Imaging with Swept-Source Optical Coherence Tomography in Patients with Birdshot Chorioretinopathy," Ophthalmology **124**(8), 1186–1195 (2017).

20. L. An and R. K. K. Wang, "In vivo volumetric imaging of vascular perfusion within human retina and choroids with optical micro-angiography," Opt. Express **16**(15), 11438–11452 (2008).

21. C. L. Chen and R. K. Wang, "Optical coherence tomography based angiography [Invited]," Biomed. Opt. Express **8**(2), 1056–1082 (2017).

22. A. H. Kashani, C. L. Chen, J. K. Gahm, F. Zheng, G. M. Richter, P. J. Rosenfeld, Y. G. Shi, and R. K. K. Wang, "Optical coherence tomography angiography: A comprehensive review of current methods and clinical applications," Prog. Retinal Eye Res. **60**, 66–100 (2017).

23. M. Adhi, D. Ferrara, R. F. Mullins, C. R. Baumal, K. J. Mohler, M. F. Kraus, J. Liu, E. Badaro, T. Alasil, J. Hornegger, J. G. Fujimoto, J. S. Duker, and N. K. Waheed, "Characterization of Choroidal Layers in Normal Aging Eyes Using Enface Swept-Source Optical Coherence Tomography," PLoS One **10**(7), e0133080 (2015).

24. K. Kurokawa, Z. Liu, and D. T. Miller, "Adaptive optics optical coherence tomography angiography for morphometric analysis of choriocapillaris [Invited]," Biomed. Opt. Express **8**(3), 1803–1822 (2017).

25. K. H. Zhou, S. Z. Song, Q. Q. Zhang, Z. D. Chu, Z. H. Huang, and R. K. K. Wang, "Visualizing choriocapillaris using swept-source optical coherence tomography angiography with various probe beam sizes," Biomed. Opt. Express **10**(6), 2847–2860 (2019).

26. W. Drexler and J. G. Fujimoto, "State-of-the-art retinal optical coherence tomography," Prog. Retinal Eye Res. **27**(1), 45–88 (2008).

27. R. K. Wang, L. An, P. Francis, and D. J. Wilson, "Depth-resolved imaging of capillary networks in retina and choroid using ultrahigh sensitive optical microangiography," Opt. Lett. **35**(9), 1467–1469 (2010).

28. H. Zhou, Z. Chu, Q. Zhang, Y. Dai, G. Gregori, P. J. Rosenfeld, and R. K. Wang, "Attenuation correction assisted automatic segmentation for assessing choroidal thickness and vasculature with swept-source OCT," Biomed. Opt. Express **9**(12), 6067–6080 (2018).

29. R. W. Knighton and G. Gregori, "The Shape of the Ganglion Cell plus Inner Plexiform Layers of the Normal Human Macula," Invest. Ophthalmol. Visual Sci. **53**(11), 7412–7420 (2012).

30. L. An, R. Wang, and U. Sharma, "Methods of reducing motion artifacts for optical coherence tomography angiography," US9759544B2, (2015).

31. W. Choi, K. J. Mohler, B. Potsaid, C. D. Lu, J. J. Liu, V. Jayaraman, A. E. Cable, J. S. Duker, R. Huber, and J. G. Fujimoto, "Choriocapillaris and Choroidal Microvasculature Imaging with Ultrahigh Speed OCT Angiography," PLoS One **8**(12), e81499 (2013).

32. H. Zhou, Y. Dai, Y. Shi, J. F. Russell, C. Lyu, J. Noorikolouri, W. J. Feuer, Z. Chu, Q. Zhang, L. de Sisternes, M. K. Durbin, G. Gregori, P. J. Rosenfeld, and R. K. Wang, "Age-Related Changes in Choroidal Thickness and the Volume of Vessels and Stroma Using Swept-Source OCT and Fully Automated Algorithms," Ophthalmol. Retina **4**(2), 204–215 (2020).

33. Q. Wang, S. Chan, J. Y. Yang, B. You, Y. X. Wang, J. B. Jonas, and W. Bin Wei, "Vascular Density in Retina and Choriocapillaris as Measured by Optical Coherence Tomography Angiography," Am. J. Ophthalmol. **168**, 95–109 (2016).

34. F. Alten, P. Heiduschka, C. R. Clemens, and N. Eter, "Exploring choriocapillaris under reticular pseudodrusen using OCT-Angiography," Graefe's Arch. Clin. Exp. Ophthalmol. **254**(11), 2165–2173 (2016).

35. J. J. Weiter, F. C. Delori, G. L. Wing, and K. A. Fitch, "Retinal-Pigment Epithelial Lipofuscin and Melanin and Choroidal Melanin in Human Eyes," Invest. Ophthalmol. Visual Sci. **27**, 145–152 (1986).

36. D. Y. Kim, J. Fingler, R. J. Zawadzki, S. S. Park, L. S. Morse, D. M. Schwartz, S. E. Fraser, and J. S. Werner, "Optical imaging of the chorioretinal vasculature in the living human eye," Proc. Natl. Acad. Sci. U. S. A. **110**(35), 14354–14359 (2013).

37. B. Braaf, K. V. Vienola, C. K. Sheehy, Q. Yang, K. A. Vermeer, P. Tiruveedhula, D. W. Arathorn, A. Roorda, and J. F. de Boer, "Real-time eye motion correction in phase-resolved OCT angiography with tracking SLO," Biomed. Opt. Express **4**(1), 51–65 (2013).

38. Y. L. Jia, S. T. Bailey, T. S. Hwang, S. M. McClintic, S. S. Gao, M. E. Pennesi, C. J. Flaxel, A. K. Lauer, D. J. Wilson, J. Hornegger, J. G. Fujimoto, and D. Huang, "Quantitative optical coherence tomography angiography of vascular abnormalities in the living human eye," Proc. Natl. Acad. Sci. U. S. A. **112**(18), E2395–E2402 (2015).

39. M. Nassisi, E. Baghdasaryan, E. Borrelli, M. Ip, and S. R. Sadda, "Choriocapillaris flow impairment surrounding geographic atrophy correlates with disease progression," PLoS One **14**(2), e0212563 (2019).

40. Q. Q. Zhang, F. Zheng, E. H. Motulsky, G. Gregori, Z. D. Chu, C. L. Chen, C. X. Li, L. de Sistemes, M. Durbin, P. J. Rosenfeld, and R. K. Wang, "A Novel Strategy for Quantifying Choriocapillaris Flow Voids Using Swept-Source OCT Angiography," Invest. Ophthalmol. Visual Sci. **59**(1), 203–211 (2018).

41. M. R. Thorell, R. Goldhardt, R. P. Nunes, C. A. D. Garcia, A. M. Abbey, A. E. Kuriyan, Y. S. Modi, G. Gregori, Z. Yehoshua, W. Feuer, S. Sadda, and P. J. Rosenfeld, "Association Between Subfoveal Choroidal Thickness, Reticular Pseudodrusen, and Geographic Atrophy in Age-Related Macular Degeneration," Ophthalmic Surg Lasers Imaging Retina **46**(5), 513–521 (2015).

42. S. M. Wang, Y. Wang, X. M. Gao, N. N. Qian, and Y. E. Zhuo, "Choroidal thickness and high myopia: a cross-sectional study and meta-analysis," BMC Ophthalmol. **15**(1), 70 (2015).

43. K. Watanabe, K. Tsunoda, Y. Mizuno, and K. Akiyama, "Outer Retinal Morphology and Visual Function in Patients With Idiopathic Epiretinal Membrane," JAMA Ophthalmol. **131**(2), 172–177 (2013).

44. S. Yoneya, M. O. M. Tso, and K. Shimizu, "Patterns of the Choriocapillaris - a Method to Study the Choroidal Vasculature of the Enucleated Human-Eye," Int. Ophthalmol. **6**(2), 95–99 (1983).

45. E. Torczynski and M. O. M. Tso, "The Architecture of the Choriocapillaris at the Posterior Pole," Am. J. Ophthalmol. **81**(4), 428–440 (1976).

46. M. Arya, A. S. Sabrosa, J. S. Duker, and N. K. Waheed, "Choriocapillaris changes in dry age-related macular degeneration and geographic atrophy: a review," Eye and Vis **5**(1), 22 (2018).

47. P. H. Tomlins and R. K. Wang, "Theory, developments and applications of optical coherence tomography," J. Phys. D: Appl. Phys. **38**(15), 2519–2535 (2005).

48. W. H. Meng, J. Butterworth, F. Malecaze, and P. Calvas, "Axial Length of Myopia: A Review of Current Research," Ophthalmologica **225**(3), 127–134 (2011).

49. A. Seidemann, F. Schaeffel, A. Guirao, N. Lopez-Gil, and P. Artal, "Peripheral refractive errors in myopic, emmetropic, and hyperopic young subjects," J. Opt. Soc. Am. A **19**(12), 2363–2373 (2002).